ACS APPLIED MATERIALS & INTERFACES

Research Article

Cite This: ACS Appl. Mater. Interfaces 2019, 11, 19141−19155

www.acsami.org

Achieving Controllable MoS_2 Nanostructures with Increased Interlayer Spacing for Efficient Removal of Pb(II) from Aquatic Systems

Neeraj Kumar,*[,†] Elvis Fosso-Kankeu,[‡] and Suprakas Sinha Ray*[,†,§]

[†]DST-CSIR National Centre for Nanostructured Materials, Council for Scientific and Industrial Research, Pretoria 0001, South Africa

[‡]Water Pollution Monitoring and Remediation Initiatives Research Group, School of Chemical and Minerals Engineering, North-West University, Potchefstroom, South Africa

[§]Department of Applied Chemistry, University of Johannesburg, Doornfontein 2028, South Africa

Supporting Information

ABSTRACT: The development of new synthesis approaches for MoS_2 is necessary to achieve controlled morphologies and unique physicochemical properties that can improve its efficiency in particular applications. Herein, a facile one-step hydrothermal route is proposed to prepare controllable MoS_2 micro/nanostructures with an increased interlayer using sodium diethyldithiocarbamate trihydrate as the new S source at different pH values. To investigate the morphology, chemical composition, and structure of the MoS_2 micro/nanostructures, various characterization techniques were used. The obtained microrods, microspheres, and microrods with hairlike structures (denoted as MoS_2-N-H) were composed of MoS_2 nanosheets with increased interlayer spacing (∼1.0 nm) and utilized for the removal of Pb(II) from aquatic systems. Among the structures, MoS_2-N-H demonstrated the highest adsorption capacity (303.04 mg/g) for Pb(II) due to the existence of −S/−C/−N/−O-comprised functional groups on its surface, which led to strong Pb−S complexation and electrostatic attractions. The uptake of Pb(II) onto MoS_2-N-H followed pseudo-second-order kinetics and Freundlich isotherm. To evaluate its practical applicability, the adsorbent was employed in real mine water analysis; it was found that MoS_2-N-H could adsorb almost 100% of the Pb(II) ions in the presence of various coexisting ions. Additionally, after Pb(II) adsorption, MoS_2-N-H was transformed into $PbMoO_{4-x}S_x$ spindlelike nanostructures, which were further used for photodegradation of an antibiotic, viz., ciprofloxacin (CIP), to avoid secondary environment waste. Thus, this investigation provides an effective one-pot approach to fabricate controllable MoS_2 micro/nanostructures with increased interlayer spacing for water treatment. The utility of these nanostructures in related supercapacitor/battery applications may also be envisaged because of their unique structural properties.

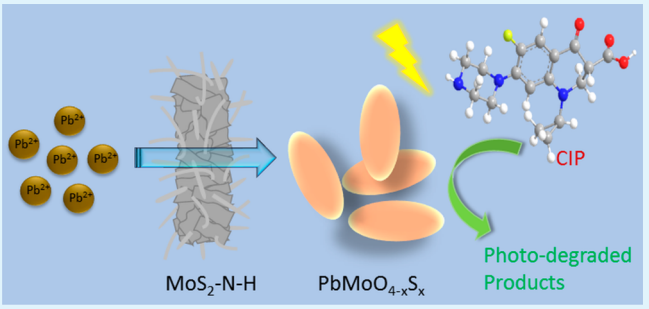

KEYWORDS: *MoS_2 nanostructure, Water purification, Lead adsorption, Photocatalysis, Ciprofloxacin, Secondary waste*

INTRODUCTION

Due to socio-economic development and urban expansion, the use of heavy metals in various industries to improve product quality has led to severe toxic metal contamination problems in water bodies.[1−3] The discharge of heavy metals (such as Hg, Pb, Cd, Ni, As, Ag, and Cr) from industrial effluents into the environment is increasing rapidly and presents a severe toxicological threat to the human body and the ecosystem. Thus, the development of facile approaches and cheap adsorbent materials for the elimination of heavy-metal ions from aquatic systems is imperative. Heavy metals can amass in biological organisms via the food web and cause human health issues by damaging the nervous system, lungs, liver, reproductive system, and kidneys.[4,5] Lead is a versatile metal that is used in numerous applications, such as storage batteries, electroplating, paints, and metal finishing.[6,7] Pb(II) ions are inevitably released into the environment; these ions are nonbiodegradable and accumulate with time. The limit set by the World Health Organisation (WHO) for Pb(II) ions in surface and potable water is less than 0.01 mg/L.[8] Thus, even very low (ppb) amounts of lead can indirectly or directly cause harm to human health. The complete elimination of heavy metals from water systems by using technologies such as membrane filtration, ion exchange, adsorption, reverse osmosis, coprecipitation, coagulation, and electro-dialysis is efficient and feasible.[9−11] Adsorption, with its simple processing, cost effectiveness, high performance, and availability, is the most preferred and widely used technique for water treatment on a small or large scale.[12,13]

Received: March 2, 2019
Accepted: May 6, 2019
Published: May 6, 2019

DOI: 10.1021/acsami.9b03853
ACS Appl. Mater. Interfaces 2019, 11, 19141−19155

Numerous adsorbents, such as nanocellulose,[14] clay,[15] activated carbon,[11] biomass,[16] hydrogels,[17] mesoporous materials,[18] and nanocomposites,[19] have been evaluated for use in the elimination of Pb(II) ions from polluted water. However, these materials present disadvantages, such as low performance, low surface area, poor selectivity, and slow kinetics. In this scenario, the development of ecofriendly and efficient new adsorbents with unique morphologies for the elimination of Pb(II) from aquatic systems is a pressing concern. Furthermore, a deeper understanding of the interactions of new materials with heavy metals is interesting from a fundamental research perspective.

Recently, the use of two-dimensional (2D) nanomaterials, such as h-BN,[20] metal chalcogenides (viz., MoS_2),[21,22] MXenes,[20] and graphene/graphene oxides,[23,24] has been considered in a wide range of environmental applications due to their high surface area and high catalytic activity. Among these, MoS_2 nanosheets have demonstrated excellent adsorption characteristics and have shown considerable potential for the elimination of heavy-metal ions from contaminated water because of their intrinsically sulfur-rich surfaces (promising binding sites) and voids or defects in their basal and edge planes.[21,25] In order to enhance adsorption and selectivity, specific interactions should occur between the adsorbate and adsorbent; such interactions can easily be achieved with MoS_2. According to Pearson's hard−soft acid−base (HSAB) theory, the S atoms present on MoS_2 act as soft bases, making their complexation with soft acids such as Pb(II), Ag(I), and Hg(II) highly favorable via strong soft−soft interactions.[26,27] MoS_2 monolayers comprise covalently attached atomic S−Mo−S trisublayers; these monolayers are joined by van der Waals forces to produce a bulk crystal. MoS_2 (naturally occurring) is isolated from molybdenite ore,[28] but it is not a suitable adsorbent due to the low interlayer spacing of 0.3 nm between adjacent layers, which restricts the ability of ionic molecules to interact with the interior S atoms.[29] Due to recent developments in synthesis approaches, 2D MoS_2 can be obtained by either solvothermal synthesis using Mo and S precursors or from the exfoliation of bulk MoS_2 to expose the abundant S atoms on the exteriors of the MoS_2 nanosheets, which results in a high number of accessible adsorption sites and consequently results in high performance. For instance, MoS_2 nanosheets with greater interlayer spacing (0.94 nm) exhibited very high Hg(II) adsorption capacity, nearly reaching the theoretical predicted adsorption capacity (~2506 mg/g). The high elimination of Hg(II) was explained by multilayer adsorption, and the mechanism was associated with the ion-exchange reaction between Hg(II) and H^+ ions on the surface of MoS_2 in aqueous solution.[29]

MoS_2 nanosheets with increased interlayer spacing are generally fabricated using a two-step process. First, MoS_2 nanosheets are synthesized by hydrothermal methods (the most commonly employed technique), exfoliation of a bulk crystal using organic/inorganic molecules, or chemical vapor deposition. Then, in the second step, the nanosheets are intercalated using alkali/alkaline elements and carbon/organic substances such as surfactants and graphene. However, these processes are cumbersome, time-consuming, and produce low yield. It is vital to develop a facile one-step route to obtain MoS_2 nanostructures with enlarged interlayer spacing. So far, MoS_2 has mainly been synthesized using thiourea, thioacetamide, cysteine, elemental S, sodium sulfide, potassium thiocyanate, or carbon disulfide as the S source; these precursors mostly form nanosheet or nanosphere/microsphere morphologies.[30−33] To achieve further advances in the MoS_2 synthesis, it is urgent to explore other potential sulfur sources for the development of new MoS_2 morphologies with unique physicochemical properties and crystal configurations. Additionally, despite the utilization of MoS_2 and MoS_2 nanohybrids as efficient adsorbents for heavy-metal elimination, the after effects of MoS_2−M^{n+} interactions on the intrinsic properties, morphology, phase, and structural transformation of MoS_2 remain mostly unexplored.

To address the needs described above, MoS_2 nanostructures with increased interlayer spacing were developed using a new sulfur source, sodium diethyldithiocarbamate trihydrate (DDC). DDC has already been used in numerous applications, such as medical applications (cancer therapy, antioxidants, bactericides), corrosion inhibition, lubrication, vulcanization accelerant, linkers, and spin trapping because of its superior chelating properties.[34] Systematic experiments were performed to understand the evolution of the various morphologies (microrods with hairlike structures, microrods, and microflowers) in the presence of DDC and EDTA at different solution pH values. The as-synthesized MoS_2 was utilized for the removal of Pb(II) ions from aquatic systems, including real mine water. Additionally, during the Pb(II) removal experiments, MoS_2 was transformed into spindlelike $PbMoO_{4-x}S_x$ nanostructures, which were further used for the photodegradation of an antibiotic, viz., ciprofloxacin, to evade secondary environment toxic waste.

EXPERIMENTAL SECTION

Materials. Sodium molybdate dihydrate (≥99%), sodium diethyldithiocarbamate trihydrate (DDC, Na as Na_2SO_4, 30.5%−32.5%), ethylenediaminetetraacetic acid (EDTA, ≥ 99%), L-arginine (≥99.5%), oleylamine (≥98%), polyethylene glycol 8000 (PEG), lead(II) nitrate (≥99.0%), and ciprofloxacin (CIP, ≥98.0%) were procured from Sigma-Aldrich. Sodium hydroxide and ethanol (99.9%) were received from Minema Chemicals.

Synthesis of MoS_2 Nanostructures. In a typical hydrothermal reaction, 0.069 M sodium molybdate dihydrate and EDTA (0.5 g) were mixed in 15 mL of deionized water. The pH of the resulting solution was adjusted to 7.0 using 2.0 M NaOH aqueous solution. After 20 min of stirring, 0.075 M DDC in 15 mL of deionized water was added to the above mixture. Subsequently, the solution was moved to a Teflon-lined hydrothermal autoclave reactor and heated at 210 °C for 24 h. The reactor was allowed to cool naturally to 25 °C, and the resulting sample was washed using water/ethanol. The sample was then dried under vacuum in an oven at 70 °C for 12 h. The product obtained under neutral conditions was denoted as MoS_2-N. The product which was synthesized using a higher concentration of DDC (0.150 M) while the other reaction parameters were maintained was referred to as MoS_2-N-H. The name MoS_2-B was given to the product that was formed under basic conditions at pH 10 while all other conditions were constant. Furthermore, the effects of different concentrations of EDTA and different capping agents (L-arginine, oleylamine, and PEG) on the evolution of the morphology of MoS_2 were studied.

Adsorption Studies. The adsorption performance of the as-prepared MoS_2 nanostructures for Pb(II) ion adsorption was determined using a batch adsorption method. Initially, the dosage and pH were optimized to achieve maximum uptake. The Pb(II) concentrations in solution before and after adsorptive removal were obtained using inductively coupled plasma-atomic emission spectrometry (ICP-AES). Isotherm experiments were conducted using various Pb(II) concentrations to determine the adsorption equilibrium. The Pb(II) solution concentrations ranging from 20 to 180 mg/L were considered to conduct adsorption isotherm experiments. A 0.025 g portion of MoS_2 nanostructures was mixed into 50 mL of Pb(II)

DOI: 10.1021/acsami.9b03853
ACS Appl. Mater. Interfaces 2019, 11, 19141−19155

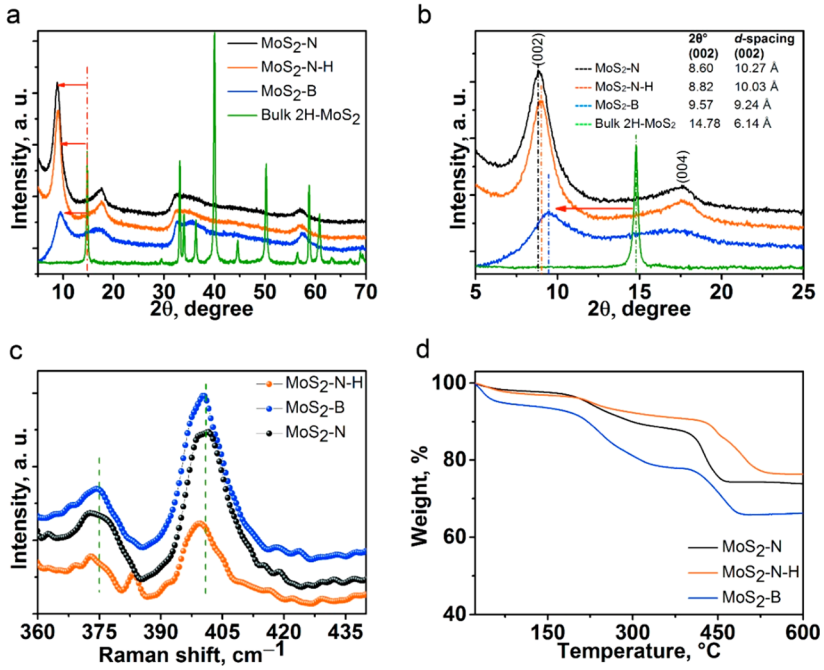

Figure 1. (a) XRD patterns. (b) Expanded view of panel (a) listing the positions of the (002) peaks and interlayer spacing distances for the MoS_2-N, MoS_2-N-H, and MoS_2-B nanostructures and the bulk 2H-MoS_2. (c) Raman spectra and (d) TGA curves for the MoS_2-N, MoS_2-N-H, and MoS_2-B nanostructures.

solution (100 mg/L); the contact time for the isotherm studies was 24 h. In the kinetics studies, 0.050 g of MoS_2 nanostructures was added to 100 mL of a Pb(II) solution (100 mg/L) and the mixture stirred vigorously from 10 min to 20 h. The contact time for interaction between the adsorbent and the adsorbate was varied to obtain the adsorption kinetics data. For the real mine water experiments, 0.050 g of the adsorbent was mixed to 100 mL of solution and stirred for 2 h. Furthermore, the mine water was spiked with 50 mg/L Pb(II) solution while all other conditions were constant to evaluate the practical utility of the present adsorbent. The removal percentage (%), distribution coefficient (K_d), and adsorption capacity (q_e, mg/g) were determined using eqs 1−3.

$$\text{removal}\ (\%) = \frac{C_0 - C_e}{C_0} \times 100 \quad (1)$$

$$q_e\ (\text{mg/g}) = \frac{C_0 - C_e}{m} \times V \quad (2)$$

$$K_d = \frac{C_0 - C_e}{C_e} \times \frac{V}{m} \quad (3)$$

where C_e and C_0 (mg/L) signify the equilibrium and initial concentrations of the Pb(II) solution, respectively. V signifies the volume of the solution (mL), and m signifies the mass (g) of MoS_2 nanostructures used. The adsorption studies were executed using a volume to mass ratio of 1000 mL/g at 25 ± 0.2 °C (unless otherwise specified).

RESULT AND DISCUSSION

Nanostructures of MoS_2 with various morphologies and increased interlayer spacing were synthesized by the hydrothermal reaction of sodium molybdate and the new sulfur precursor DDC at different pH values. The XRD patterns obtained from the products MoS_2-N, MoS_2-N-H, and MoS_2-B were completely different from that of bulk 2H-MoS_2 (Figure 1a,b). The observed XRD peaks matched well with the standard peaks of MoS_2 (JCPDS 37-1492).[31] The intense and narrow diffraction peak at 14.78° in bulk MoS_2 corresponded to the (002) diffraction plane with an interlayer spacing of 6.14 Å, whereas a significant shift and broadening of the (002) diffraction plane were observed for the MoS_2 nanostructures (Figure 1a). The shifting of the (002) peak toward lower 2θ values could be attributed to lattice expansion in the c-axis direction and intercalation of molecules between layers of MoS_2.[35] The interlayer spacing between adjacent sheets of MoS_2-N, MoS_2-N-H, and MoS_2-B was expanded to 10.27, 10.02, and 9.24 Å, respectively (Figure 1b). Less interlayer expansion in MoS_2-B occurred due to initially high incorporation of hydroxyl groups in S−Mo−S layers in basic condition, which later become repulsive to bigger molecules and consequently lower expansion. Moreover, the appearance of new peaks at ∼17.7° was related to the (004) plane and reaffirmed the lattice expansion of the MoS_2 nanostructures. The broadness of the (002) and (004) peaks indicated the intercalation of heteromolecules, with random sheet stacking and low crystallinity.[29,36] The increased interlayer spacing probably occurred due to the in situ intercalation of Na, hydrated Na, $Na_2SO_4/(NH_4)_2SO_4$, NH_3/NH_4^+, and $R_2H_2N^+$ between S−Mo−S layers of MoS_2.

The Raman spectra of the MoS_2-N, MoS_2-N-H, and MoS_2-B nanostructures exhibited two characteristic broad peaks at 401 and 375 cm^{-1}, which were ascribed to out-of-plane A_{1g} and in-plane E^1_{2g} vibrational modes of 2H-MoS_2, respectively (Figure 1c).[37] A red-shift and broadening of the peaks were observed due to the smaller size of the layers and the multilayer curved structure of the MoS_2 nanoflakes. In the MoS_2-N-H spectrum, the extra peak that appeared at 383.4 cm^{-1} was tentatively associated with the S═C−S stretch of DDC.[38] Moreover, the comparatively higher intensity of the A_{1g} mode than the E^1_{2g} mode indicated that the MoS_2 nanosheets were rich in edge-terminating structures.[39,40]

The TGA plots for the MoS_2-N, MoS_2-N-H, and MoS_2-B nanostructures are shown in Figure 1d. The weight loss observed below 200 °C was ascribed to the release of water. The weight

DOI: 10.1021/acsami.9b03853
ACS Appl. Mater. Interfaces 2019, 11, 19141−19155

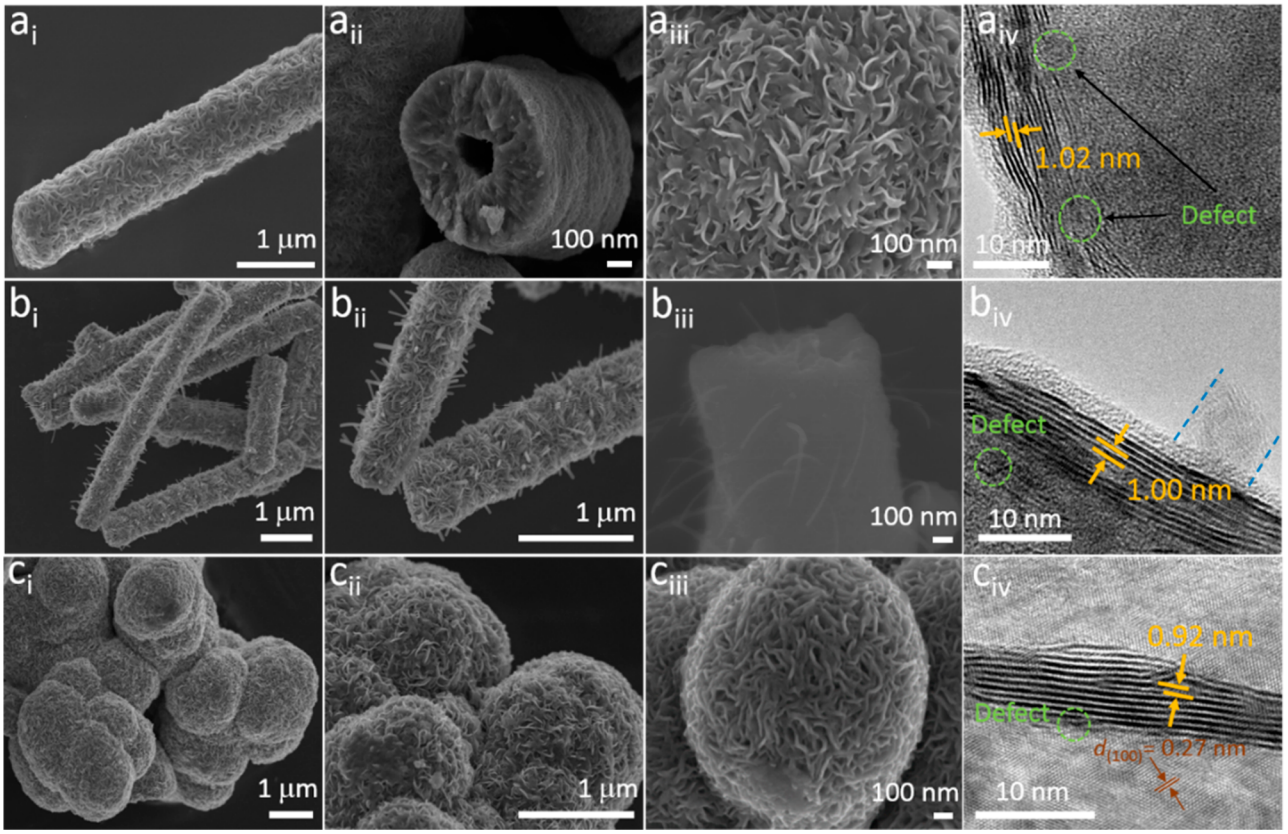

Figure 2. SEM images of (a_i–a_{iii}) MoS_2-N, (b_i–b_{iii}) MoS_2-N-H, and (c_i–c_{iii}) MoS_2-B at three levels of magnification. HRTEM images of (a_{iv}) MoS_2-N, (b_{iv}) MoS_2-N-H, and (c_{iv}) MoS_2-B, highlighting the interlayer spacing and defects.

loss in the range of 200–360 °C was attributed to loss of NH_3, H_2S, and organic ligands such as EDTA and DDC on the surfaces of the MoS_2 structures.[41] The sharp decline in weight from 385 to 490 °C occurred due to the combustion of carbon moieties. For the MoS_2-N-H sample, this range extended from 400 to 550 °C, agreeing with the presence of additional carbon in the matrix due to the high concentration of DDC. Above 550 °C, no weight loss was observed for any of the three samples, suggesting that only MoS_2 existed in this range. The overall weight loss was higher (i.e., lower thermal stability) in the case of MoS_2-B than MoS_2-N-H and MoS_2-N due to the low availability of char residues on the surface as it carried fewer functional moieties (EDTA and DDC), which was later reaffirmed by FTIR results. The greater residual moisture of MoS_2-B could be ascribed to the excess hydroxyl groups incorporated between S–Mo–S layers due to the highly basic system.

The morphologies of MoS_2-N, MoS_2-N-H, and MoS_2-B were examined using FESEM and TEM. Figure 2a_i–a_{iii} exhibits the FESEM images of MoS_2-N (synthesized under neutral pH conditions) at different magnifications, in which hollow microrod structures comprising uniformly self-arranged MoS_2 nanosheets are observed. These microrods had lengths of 4–7 μm and widths ranging from 800 nm to 2.0 μm. For the MoS_2 prepared using a high concentration of DDC (MoS_2-N-H), a bacteria-like structure with pili (hairlike structures) on the surface was achieved, as shown in Figure 2b_i–b_{iii}. The surfaces of these microrods exhibited a bacteria-like structure and were also composed of loosely packed uniform MoS_2 nanoflakes.

The hairlike structures were 200–400 nm long and 10–50 nm wide and were possibly composed of carbon-containing materials. These hairlike structures grew on the surface through the nanosheets of MoS_2 (Figure 2b_{iii}). Additionally, the EDX spectrum indicated that MoS_2-N-H was composed of the elements Mo, S, C, O, and Na, and the EDX mapping highlighted the homogeneous distribution of Mo and S throughout the entire sample [Figure S1, Supporting Information (SI)]. The C, O, and Na elements were ascribed to the occurrence of residual EDTA and DDC on the surface of MoS_2 and the hairlike structures. For the nanostructures synthesized in a basic medium (MoS_2-B), flowerlike microspheres with a diameter of 1–2 μm were observed. The nanospheres consisted of self-assembled MoS_2 nanosheets with sharp edges similar to flower petals (Figure 2c_i–c_{iii}). HRTEM images revealed that the as-synthesized nanostructures were composed of multilayer MoS_2 nanoflakes. As indicated in panels a_{iv}, b_{iv}, and c_{iv} of Figure 2, MoS_2-N, MoS_2-N-H, and MoS_2-B consisted of stacked MoS_2 nanosheet layers with an interlayer spacing of 1.02, 1.0, and 0.92 nm, respectively; these results were similar to those obtained from the XRD patterns. It is evident that all morphologies contained discontinuous MoS_2 nanosheets, which implied the presence of a large number of crystallographic defects. In the case of MoS_2-N-H, the HRTEM image (Figure 2a_{iv}) demonstrated an amorphous budding (hairlike) structure, which was related to the carbon material. During electron beam irradiation, these hairlike structures on MoS_2 became depleted or began to decompose, which suggested their low stability and amorphous carbon characteristics (Figure S2, SI). As indicated in Figure 2c_{iv}, the lattice fringes (0.27 nm) present in the basal plane were consistent with the crystal spacing of the (001) plane. Moreover, the lattice fringe orientation was not consistent over the whole basal surface and rotated slightly from one region to another, which further

DOI: 10.1021/acsami.9b03853
ACS Appl. Mater. Interfaces 2019, 11, 19141–19155

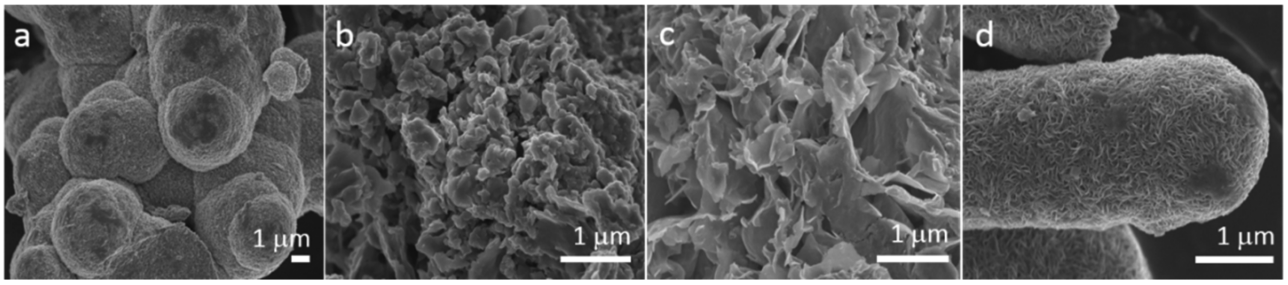

Figure 3. Surface morphologies (FE-SEM images) of MoS_2 synthesized using DDC as the S source in the presence of different capping agents: (a) L-arginine, (b) oleylamine, (c) PEG, and (d) EDTA.

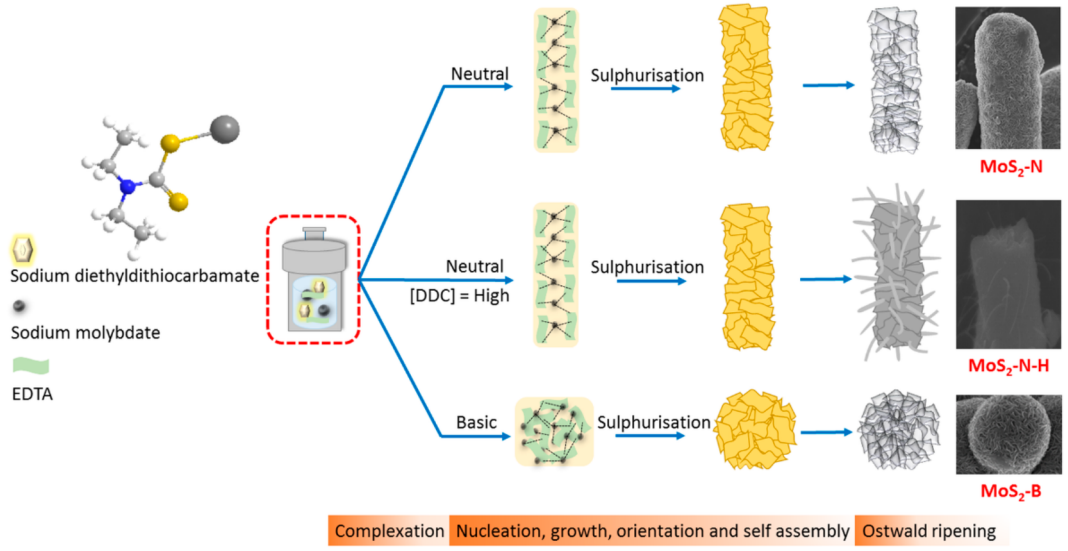

Figure 4. Schematic showing the formation mechanisms of the MoS_2 nanostructures.

supported the presence of defects in the basal plane and a different arrangement of stacked sheets.

Synthesis Mechanism of the Various Morphologies of MoS_2. To obtain distinct morphologies in a controlled fashion, the new sulfur source DDC was selected for the preparation of MoS_2 nanostructures. Initially, the reaction was performed in ethanol using a stoichiometric concentration of sodium molybdate and DDC. As expected, the morphology of the resulting product was uneven and irregular (Figure S3, SI). Later, water was selected as the solvent, and the reaction was performed using different concentrations of DDC. The crystal structure of the as-prepared MoS_2 was in agreement with that of 2H-MoS_2 (see XRD results in Figure S4, SI). Microflakes of MoS_2 were observed when a stoichiometric ratio of the precursors was used, whereas with a high concentration of DDC, microflakes with nanosized hairlike spikes were obtained. The excess DDC might possibly be incorporated into the nanosized hairlike spike structures on the surface of MoS_2 (as shown in Figure S5, SI).

Additionally, EDX mapping was employed to investigate the composition of the hairlike structures. The EDX mapping results indicated that these structures were not comprised of MoS_2, but instead of C and Na, which are present in DDC (Figure S6, SI). Furthermore, these hairlike structures were unstable under the electron beam due to their thinness and their composition, which made it difficult to obtain enough counts to produce good EDX maps. To further explore the possible morphologies, various reactions were carried out using capping agents such as arginine, oleylamine, PEG, and EDTA, which led to the formation of microspheres, microflakes, microsheets, and microrods, respectively (Figure 3). As EDTA produced unusually well controlled microrods of MoS_2, it was utilized in the rest of the studies. EDTA is not soluble in water. NaOH was mixed into the solution to solubilize EDTA, resulting in a pH of 7 in the reaction mixture. Thus, the MoS_2 microrods were synthesized under neutral pH conditions, and their structural growth was controlled by OH^-, NH_4^+, and H^+ ions and the EDTA binding effect.[42,43] Under basic conditions (pH ~10), microspheres of MoS_2 were obtained due to the high amount of OH^- ions and the different nature of the chelation of EDTA to Mo.

Moreover, the effect of the EDTA concentration on the morphology was studied by changing the concentration of EDTA in the reaction (Figure S7, SI). The microrods of MoS_2 began to join with one another as the EDTA concentration was increased from 1.0 to 3.0 g, and the assembled nanosheet layers on their surface became thicker, which consequently reduced the porosity of the MoS_2 structures. Thus, EDTA played a vital role in the evolution of the MoS_2 structures, and a low concentration of EDTA (0.5 g) was used for all further reactions. The formation of the microrods and microflowers can be explained via the following mechanisms (Figure 4): first, in the formation of microrods of MoS_2, sodium molybdate reacts with EDTA during the dissolution process at neutral pH to form coordinated Mo−EDTA complexes, possibly of the form $[(H_2EDTA)Mo_2O_6(H_2EDTA)]\cdot 2H_2O$, in which the cation

DOI: 10.1021/acsami.9b03853
ACS Appl. Mater. Interfaces 2019, 11, 19141−19155

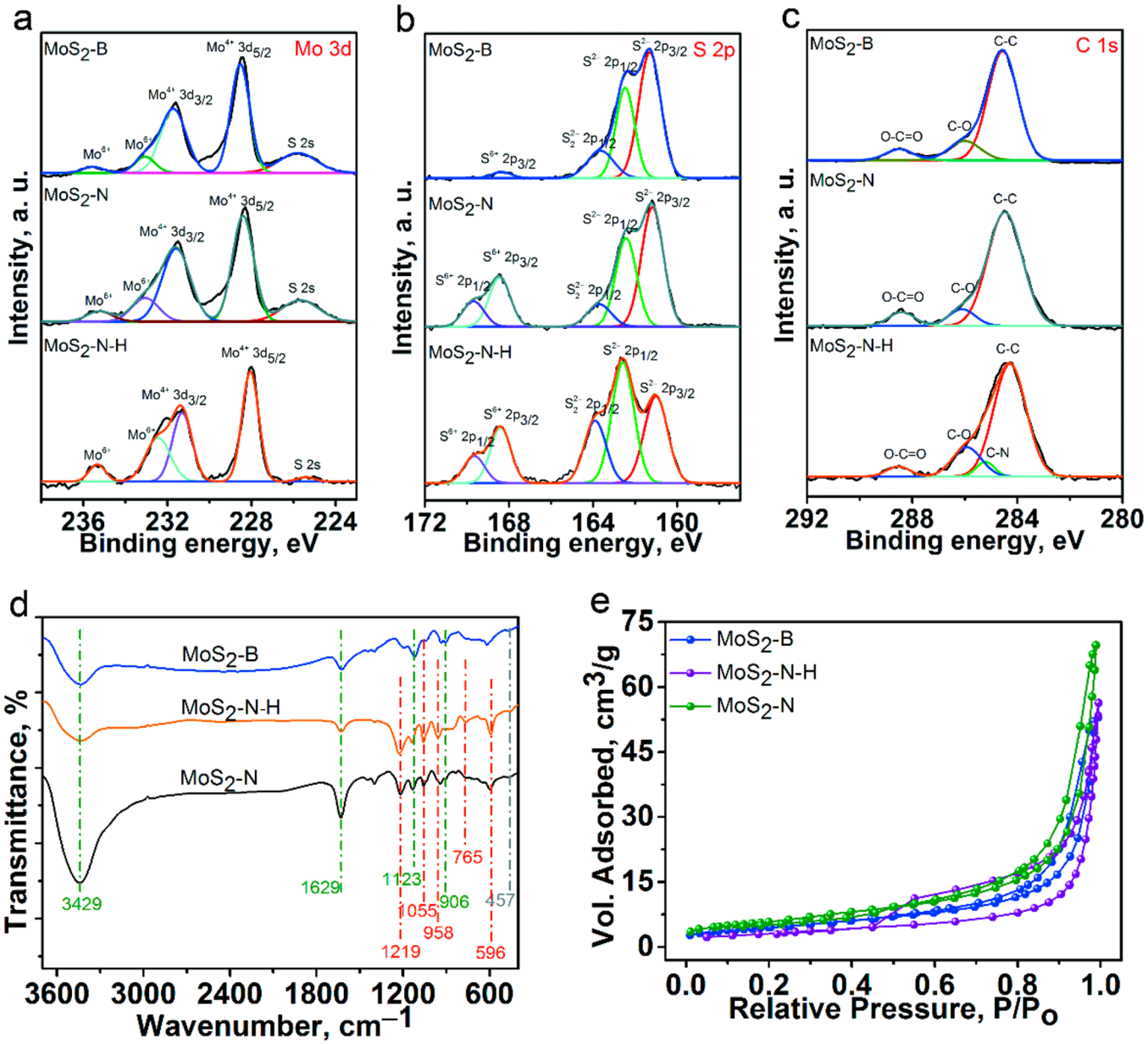

Figure 5. XPS spectrum of MoS_2-N, MoS_2-N-H, and MoS_2-B. (a) Mo 3d spectra, (b) S 2p spectra, and (c) C 1s spectra. (d) FTIR and (e) BET isotherms for MoS_2-N, MoS_2-N-H, and MoS_2-B.

and the anion are linked via N−H···O−Mo interactions to create one-dimensional chain or rod structures.[44,45] Later, sulfurization occurred with the help of DDC molecules, which provide CS_2 to form MoS_2 microrods. In case of the microflowers, the formation of a coordinated Mo−EDTA complex possibly occurred as $[\{Na_4(H_2O)_8\}\{Mo_2O_6(EDTA)\}]$; these complexes could then link with one another via C−H···O−Mo interactions to form zigzag structures. These structures could then further interconnect through Na−O bonds.[44] During sulfurization using DDC, the zigzig structures might be converted into a microsphere-like morphology. Overall, the formation of MoS_2 begins with a complexation reaction between EDTA and Mo and nucleation via a sulfurization process using DDC, followed by growth, orientation, self-assembly, and finally Ostwald ripening processes to yield MoS_2 structures with controlled morphologies. For the MoS_2-N-H sample, the excess DDC might be converted into the hairlike structures on the MoS_2 structures. EDTA also restricts the formation of side products such as molybdenum oxide by forming a stable complex with Mo, which prevents the reaction of Mo with the OH^- in solution.

To further investigate the chemical states and composition of synthesized MoS_2 nanostructures, XPS measurements were performed. As shown in the survey spectrum (Figure S8, SI), MoS_2 nanostructures demonstrated the characteristic peaks of S (2p), Mo (3p, 3d, 4p), C (1s), O (1s, KLL), and Na (1s, 2s, KLL). The peaks related to C, O, and Na could be ascribed to the residual of EDTA and DDC on the surface of MoS_2 nanostructures. In MoS_2-N-H, the increased peak intensity of C 1s and Na 1s, and the appearance of the N 1s peak suggested the availability of DDC as hairlike structures within the MoS_2 nanorods. In Mo 3d spectra (Figure 5a), the doublet peaks centered at lower binding energy (~231.6 and ~228.5 eV) were related to Mo^{4+} $3d_{3/2}$ and $3d_{5/2}$ of MoS_2, respectively. The

DOI: 10.1021/acsami.9b03853
ACS Appl. Mater. Interfaces 2019, 11, 19141−19155

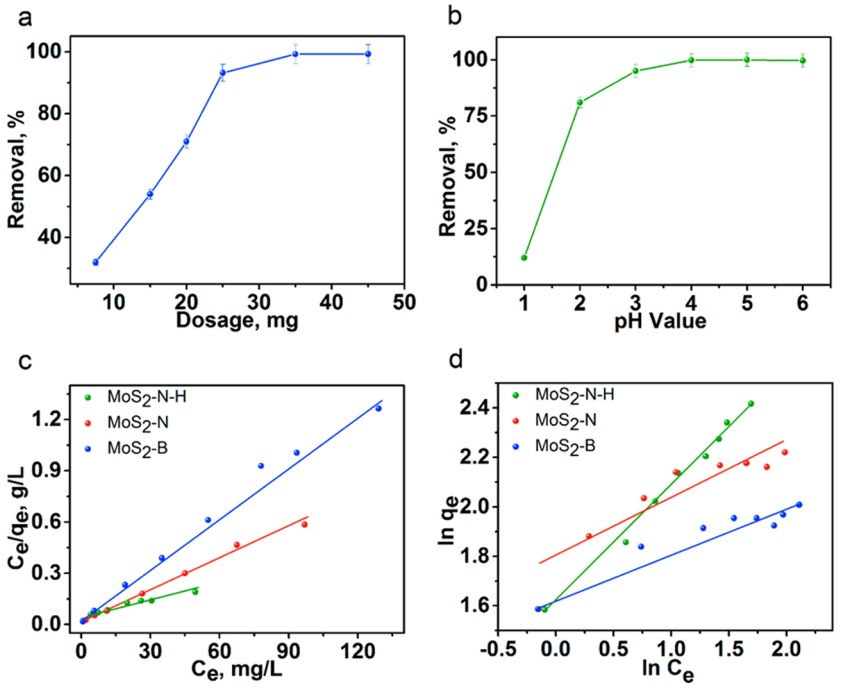

Figure 6. (a) Effect of MoS_2-N dosage on the removal of Pb(II) ions. (b) Effect of pH on the adsorption performance of MoS_2-N. (c) Langmuir and (d) Freundlich isotherms for the adsorption of Pb(II) ions on the MoS_2-N, MoS_2-N-H, and MoS_2-B nanostructures.

higher binding energy peaks located at ~233.1 and ~235.6 eV belonged to unreduced Mo^{6+}. In MoS_2-N-H, peaks mentioned above shifted to lower binding energy, suggesting structure complexity. In the S 3p spectra (Figure 5b), the obtained doublet for S $2p_{3/2}$ and S $2p_{1/2}$ at ~161.5 and ~162.4 eV was ascribed to the S^{2-} of MoS_2.[31] The peak centered at ~163.8 could be assigned to bridging S_2^{2-}.[46] The peaks positioned at ~168.4 and ~169.7 eV corresponded to S^{6+} $2p_{3/2}$ and $2p_{1/2}$ of SO_4^{2-} respectively, which might be attributed to intercalation of sodium sulfate/ammonium sulfate between the MoS_2 layers during the synthesis. This resulted in the increased interlayer spacing of MoS_2 nanostructures. The S 2p spectrum of MoS_2-N-H did not show the evident spin−orbit splitting, suggesting that the oxidation states of S atoms in MoS_2-N-H were complicated. The lower binding energy peaks (161.1 and 162.6 eV) could be assigned to unsaturated S^{2-} of MoS_2, whereas the higher binding energy peak at 164.0 eV could be accredited to the bridging S_2^{2-} and/or apical S^{2-} of MoS_2.[46] In Figure 5c, the high-resolution scan of C 1s demonstrated numerous peaks of oxygen and nitrogen functionalities. The peaks located at ~284.6, ~286.0, and ~288.9 eV were ascribed to C−C, C−O, and O−C═O, respectively, suggested the presence of EDTA/DDC on the surface.[47] An additional peak at 285.3 eV in MoS_2-N-H originated from C−N bonds due to the high concentration of DDC.[47,48]

FTIR measurements were carried out to investigate the functional moieties linked to the surfaces (Figure 5d). The broad vibrational band at 3429 cm^{-1} corresponded to O−H stretching. The peaks at ~2980 cm^{-1} were attributed to the CH_2 stretching of the alkyl groups of EDTA and DDC. The bands at 1629, 1392, 1123, and 1055 cm^{-1} were assigned to the C═O stretching, C−H bending, C−O stretching, and C−N stretching, respectively, of the EDTA moieties attached to all three samples.[49] Additionally, the peaks at 1219, 958, 906, and 765, and 596 cm^{-1} corresponded to the respective C−C stretching, C−N stretching, in-plane C−H bending, out-of-plane C−H bending, and S−S stretching (due to bond formation between the S atoms of MoS_2 and DDC) of the DDC molecules.[50] The intensity of the peaks of the DDC molecules was higher in the MoS_2-N-H spectrum than in that of MoS_2-N, which supported our previous observation that excess DDC was present on the surface of MoS_2-N-H as hairlike structures. The weak characteristic band at 457 cm^{-1} was related to S−Mo stretching, indicating the successful formation of MoS_2 nanostructures. The BET specific surface areas of the as-prepared MoS_2 nanostructures were obtained from their N_2 adsorption−desorption isotherms (Figure 5e). The microrod MoS_2 structures (MoS_2-N, MoS_2-N-H) exhibited higher surface areas and pore volumes than the MoS_2 microspheres (MoS_2-B) (Table S1 and Figure S9, SI). The surface area, pore volume, and pore size for MoS_2-N-H were calculated to be 17.083 m^2/g, 0.094 cm^3/g, and 12.28 nm, respectively. The surface area of as-prepared MoS_2 nanostructure was higher than that of bulk MoS_2 and comparable or higher to some of the previously reported values.[31,51−53] The high surface area and pore volume indicated that the microrod MoS_2 structures might demonstrate high adsorption capability toward Pb(II).

Adsorption Studies of the MoS_2 Nanostructures. To obtain maximum Pb(II) adsorption capacity, the adsorbent dosage and pH of the reaction were optimized. Due to their high surface area, MoS_2-N microrods were utilized to optimize the parameters for the adsorption of Pb(II) ions from aqueous solutions. First, various dosages of MoS_2-N were mixed into a 100 mg/L Pb(II) solution, and the Pb(II) uptake (%) was calculated (Figure 6a). The removal efficiency initially increased with increasing microrods dosage and then reached equilibrium at a certain value. The almost-constant adsorption at high dosage occurred due to the increase in the diffusion path and the aggregation of the active sites of the adsorbent. Therefore, the optimal dosage was determined to be 0.025 g/L.

Furthermore, the effect of pH on the adsorption efficiency was studied by preparing solutions of Pb(II) with different pH

DOI: 10.1021/acsami.9b03853
ACS Appl. Mater. Interfaces 2019, 11, 19141−19155

Table 1. Evaluated Fitting Parameters and Related Error Values for Each of the Adsorption Isotherm Models

model	parameter	MoS_2-B	MoS_2-N	MoS_2-N-H
Langmuir	q_m (mg/g)	99.10	163.93	303.04
	K_L (L/mg)	2.42×10^{-1}	3.32×10^{-1}	7.87×10^{-2}
	R_L	0.023−0.172	0.016−0.131	0.066−0.389
	R^2	0.9879	0.9938	0.9409
Freundlich	K_F (L/mg)	5.27	5.81	6.16
	$1/n$ (mg/g)	0.167	0.261	0.474
	R^2	0.9089	0.8501	0.9925
Temkin	β (mg g^{-1})	10.80	17.535	53.40
	K_T (L mg^{-1})	74.3	12.25	1.44
	R^2	0.966	0.962	0.886
DKR	q_D (mg g^{-1})	87.10	137.4142	155.98
	K_{DR} (mol^2 J^{-2})	1.70×10^{-7}	2.83×10^{-7}	3.62×10^{-7}
	E_s (kJ mol^{-1})	1.72	1.33	1.18
	R^2	0.862	0.877	0.583

values; the adsorption followed a trend similar to that in the dosage experiments with increasing pH (Figure 6b). The pH has a significant effect on forms of the metal ions present in the solution and on the nature of the chemically active adsorbent sites. High pH (>6) led to the precipitation of Pb(II) as $Pb(OH)_2$.[54] Thus, the adsorption performance of MoS_2-N versus pH was examined in the acidic region only (pH 1−6). As shown in Figure 6b, the adsorption of Pb(II) on MoS_2-N initially increased drastically with increasing solution pH and then plateaued above pH 3.5. The weak adsorption of Pb(II) at low pH may be related to electrostatic repulsion and competition between the excess H^+ and Pb(II) ions for the adsorption sites. At high pH, the adsorption of Pb ions was governed by electrostatic interactions between the negative surface of the adsorbent and the positive Pb(II) ions. These observations were further sustained by ζ-potential data of MoS_2-N at different pH values from 1 to 6 (Figure S10, SI). The isoelectric point or point zero charges (pzc) for MoS_2-N was determined to be 1.15. When pzc > pH (strongly acidic conditions), the surface of the adsorbent carries positive charges that have a repulsive characteristic toward cationic molecules, consequently reducing the adsorption of Pb(II). At pH > pzc, the surface of adsorbent is negatively charged, and this charge increased on increasing pH value. The negative surface of adsorbent is appropriate for adsorption of Pb(II) ions. At low pH values, adsorption suffered from healthy competition of Pb(II) with H^+, whereas at high pH value this competition has almost vanished, which resulting in high removal of Pb(II). The best pH for the uptake of Pb(II) was found to be 5, which allowed for almost 100% uptake and a high value of K_d (>2.0×10^5 mg/L) due to the highly negatively charged surface (ζ-potential = −32.6 mV). With these observations in mind, all further adsorption experiments were performed at pH 5.

Adsorption Isotherm Studies. Adsorption isotherm experiments were performed to quantitatively analyze the adsorption characteristic of Pb(II) on the MoS_2 nanostructures and to gain a deeper understanding of the adsorption mechanism. The experimental adsorption isotherm data were fitted to commonly used models, viz., the Langmuir and Freundlich models. These models can be mathematically defined by the following equations[47]

Langmuir isotherm model

$$\frac{C_e}{q_e} = \frac{1}{K_L q_m} + \frac{C_e}{q_m} \quad (4)$$

Freundlich isotherm model

$$\log q_e = \frac{1}{n} \log C_e + \log K_F \quad (5)$$

where C_e (mg/L) and q_e (mg/L) have already been defined in the previous section, q_m (mg/g) signifies the maximum adsorption capability. $1/n$ refers to the degree of heterogeneity between adsorption and solution concentration, and K_F (L/mg) is the Freundlich constant, which relates to the adsorption driving force. K_L (L/mg) signifies the Langmuir equilibrium constant, which relates to the affinity of the binding sites. Furthermore, the Langmuir isotherm model considers monolayer adsorption, in which adsorption ensues on identical sites of a homogeneous surface. However, in the Freundlich isotherm model, multilayer adsorption takes place on heterogeneous surfaces.

The adsorption capacities of the MoS_2-N, MoS_2-N-H, and MoS_2-B nanostructures were higher for lower initial concentrations of the Pb(II) solution and lower at higher initial Pb(II) concentrations. This was attributed to an excess of available active adsorption sites at lower Pb(II) concentration, while at higher concentrations, these sites became saturated with Pb(II) ions, which consequently led to adsorption equilibrium (Figure S11, SI). The adsorption isotherm data were further fitted to Temkin and Dubinin−Kaganer−Radushkevich (DKR) models (Figure S12, SI) and their details are shown in Table S2 (SI). The experimental values, correlation coefficients (R^2), and fitted parameters for the Freundlich, Langmuir, Temkin, and DKR isotherms are listed in Table 1. The experimental data for the MoS_2-N and MoS_2-B nanostructures were the best fit with the Langmuir isotherm, which had a much higher value of R^2 (>0.98) than the other isotherms (Figure 6c,d). Additionally, the obtained value of the separation factor (R_L) for the MoS_2-N and MoS_2-B nanostructures was less than 1, which also confirmed the applicability of the Langmuir model and suggested monolayer adsorption of Pb(II). The Pb(II) adsorption data for MoS_2-N-H (the microrods with hairlike structures) were better fitted by the Freundlich model (R^2 = 0.9925) than by the Langmuir (R^2 = 0.9409), Temkin (R^2 = 0.886), and DKR (R^2 = 0.583) models. Therefore, the adsorption of Pb(II) occurred in a multilayer fashion on the

DOI: 10.1021/acsami.9b03853
ACS Appl. Mater. Interfaces 2019, 11, 19141−19155

heterogeneous surface of MoS_2-N-H. The calculated maximum adsorption capacities for Pb(II) on the MoS_2-N, MoS_2-N-H, and MoS_2-B nanostructures were 163.93, 303.04, and 99.10 mg/g, respectively. The high adsorption capacity of MoS_2-N-H could be ascribed to its excess S, O, and C functionalities and enhanced sulfur−lead complexation. Additionally, the adsorption results were supported by the surface charge on the adsorbents, which was determined by ζ-potential measurements. The ζ-potential value of MoS_2-N, MoS_2-N-H, and MoS_2-B was determined to be −33.2, −44.7, and −26.8 mV at pH 5, respectively (Figure 7). Compared to other nanostructures,

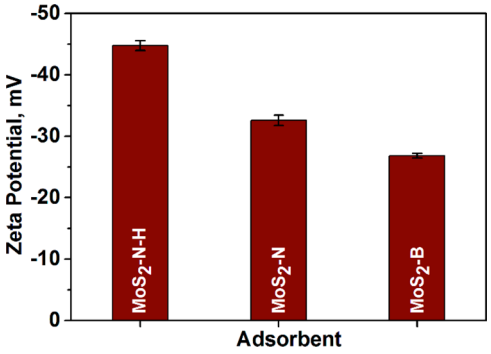

Figure 7. ζ-Potential of MoS_2-N, MoS_2-N-H, and MoS_2-B at pH 5.

MoS_2-N-H carries a highly negative surface (ζ-potential = −44.7 mV) charge, which is good for high interaction with Pb(II) ions and results in high removal capacity. Moreover, the nature of adsorption can be explained by the DKR isotherm model. The calculated value of E parameters for MoS_2-N, MoS_2-N-H, and MoS_2-B was found to be in the range of 1.18−1.72 kJ mol^{-1}, which occurs in the range of 1−8 kJ mol^{-1}, suggesting the physical adsorption of Pb(II) on the adsorbents. A comparison of lead elimination performances of as-prepared MoS_2 nanostructures with those of formerly reported metal sulfide-based adsorbents is summarized in Table 2. In comparison to the

Table 2. Comparison of the Maximum Pb(II) Removal Capacity of Various Sulfide-Based Adsorbents

adsorbent	pH	q_m(mg/g)	ref
SnS nanoparticles−activated carbon	4.0	48.5	55
MoS_2/rGO	5.0	384.16	56
MoS_2	6.8	108	57
MoS_2@biochar	5.0	189	58
CuS nanorods−activated carbon	6.0	146	59
β-cyclodextrin/Fe_3S_4	6.0	256	60
MoS_4-polypyrrole	2.5−6.0	78	61
MoS_2 microflowers	5.0	99.10	this study
MoS_2 microrods	5.0	163.93	this study
MoS_2 microrods/C	5.0	303.04	this study

earlier studies, MoS_2-N-H exhibited superior adsorption capabilities for the removal of Pb(II) from water. From Table 2, the MoS_2/reduced graphene oxide (rGO) composite (384.16 mg/g) has demonstrated a higher adsorption capacity than MoS_2-N-H nanostructures (303.04 mg/g). The high adsorption capacity of MoS_2/rGO for Pb(II) was ascribed to the excess oxygen functionalities (viz., −OH, −COOH) supplied by rGO, which enabled surface complexation, and to the negative charged surface of MoS_2 and rGO for electrostatic attractions. On the other hand, MoS_2-N-H is lacking the excessive oxygen-carrying functionalities but still showed significant Pb(II) removal capacity. The observations demonstrated the potential of the MoS_2 nanostructures for the uptake of Pb(II) from polluted water/mine water.

Kinetic Studies. On the basis of its high adsorption capacity, MoS_2-N-H was selected for further detailed studies of its adsorption kinetics. Herein, three commonly used kinetics models, intraparticle-diffusion, pseudo-first-order, and pseudo-second-order models, were chosen for fitting the experimental adsorption kinetics data. The kinetics equations and their associated parameters are summarized in Table S3 (SI). The pseudo-first-order kinetics model emphasizes that the adsorption occurs by the diffusion process, while the pseudo-second-order model considers adsorption to be determined by the square of unoccupied vacancies on the adsorbent surface and controlled by a chemisorption process that involves strong chemical interactions. The intraparticle diffusion kinetics model emphasizes that the adsorption process occurs via diffusion of the adsorbate to the inside of the particles, with the diffusion process being the rate-determining step of adsorption. To determine the relationship between time and the initial Pb(II) concentration, the graph of the adsorption capability (q_t) versus time was plotted (Figure 8a). The adsorption of Pb(II) onto MoS_2-N-H increased rapidly during the initial 150 min due to the excess of reactive moieties on the surface and then slowed close to the adsorption equilibrium, which was due to the diffusion of ions into interior pores and slow interactions between S and Pb(II) ions. The calculated kinetics parameters of the three kinetics models are shown in Table S4 (SI). The pseudo-second-order kinetics model was found to fit the data best, as it had the highest R^2 value (0.999) (Figure 8b,c).

Moreover, the theoretical value of q_e calculated using the pseudo-second-order kinetics model was better matched to the actual adsorption capacity than those calculated using the other kinetics models. Thus, the adsorption of Pb(II) on MoS_2-N-H followed pseudo-second-order kinetics, suggesting that the available surface active sites might be the rate-determining factor. As shown in Figure 8d, the q_t vs $t^{0.5}$ curve (intraparticle-diffusion curve) exhibits two linear regions. The first region corresponds to interface or film penetration, while the second region represents the diffusion of the Pb(II) ions inside the pores to slowly reach the equilibrium phase. It was observed that the intraparticle-diffusion graph was not passing through the origin, suggesting that the reaction rate could not be explained by the intraparticle kinetics model alone.

Adsorption of Pb(II) Ions from Real Mine Water. Mine water was collected from a mine near Potchefstroom, South Africa. As shown in Table S5 (SI), mine water contained different concentrations of various elements and had a pH of ∼7.08, electrical conductivity of ∼116 mS/cm, and turbidity of ∼1.27 NTU. In addition to Pb(II) ions, the real mine water contained Ca, Mg, Na, K, Cu, Fe, Ni, Ti, Si, and Sr. As demonstrated in Figure 9, the MoS_2-N-H sample easily achieved complete adsorption of the Pb(II) ions (∼100%) from the real mine water. The adsorbent also effectively adsorbed the other ions that were present in the mine water. Furthermore, after spiking the mine water with 50 mg/L of Pb(II), MoS_2-N-H (50 mg of adsorbent) could still effectively adsorb all of the Pb(II) ions from the mine water in the presence of the coexisting cations. The presence of Pb ions was also observed to enhance the removal of other metal ions. Therefore, MoS_2-N-H has strong potential to be utilized in the pollutant removal processes of real mine water and other industrial wastewater.

DOI: 10.1021/acsami.9b03853
ACS Appl. Mater. Interfaces 2019, 11, 19141−19155

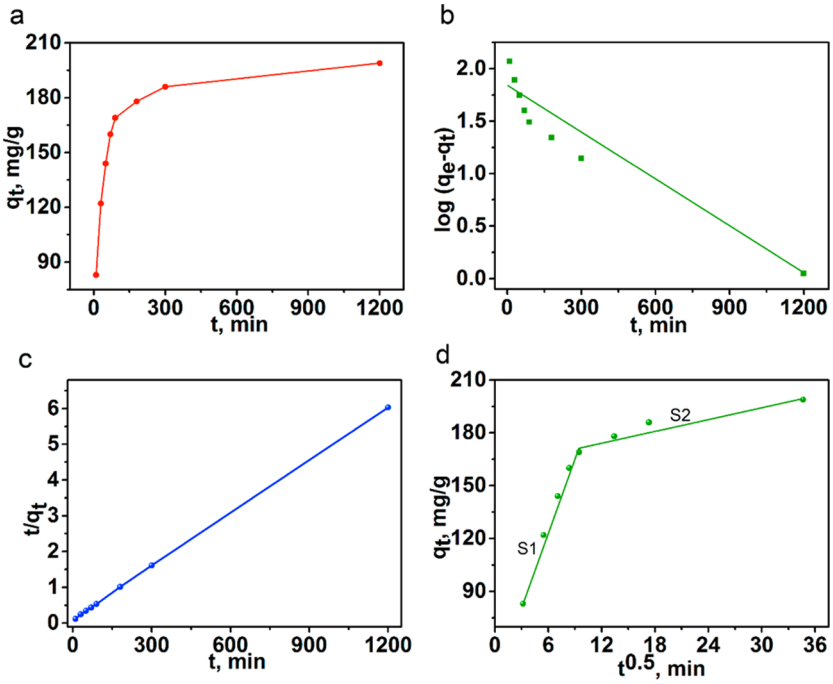

Figure 8. Plots of the (a) adsorption kinetics, (b) pseudo-first-order model, (c) pseudo-second-order model, and (d) intraparticle-diffusion model for the adsorption of Pb(II) ions.

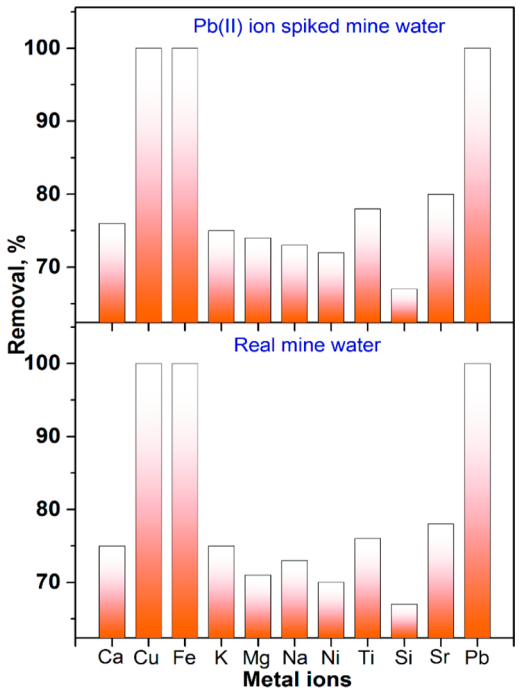

Figure 9. Removal efficiency of Pb(II) and other coexisting cations from real mine water and Pb(II) ion-spiked mine water.

The mechanism of Pb(II) adsorption on MoS_2-N-H could be attributed to ion exchange between Pb(II) and the H^+ ions that exist on the MoS_2 surface in aqueous solution, followed by complexation. As suggested by the isotherm studies, Pb(II) was adsorbed onto MoS_2-N-H via multilayer adsorption, in which the initial layer is ascribed to the chemical complexation of Pb(II) with S (inner-surface complex), whereas the second layer is associated with electrostatic interactions between Pb(II) and carbon or sulfur functionalities. Figure S13 (SI) illustrates the adsorption mechanism for Pb(II) onto MoS_2-N-H. Previous literature on the removal of heavy-metal ions on MoS_2 has also described a similar metal−sulfur complexation mechanism.[21,62]

Fate of MoS_2 after Adsorption of Pb(II) Ions. After Pb(II) adsorption studies, MoS_2-N-H sample was characterized using XRD, XPS, SEM-EDX, and TEM to understand the structural and morphological changes. The obtained XRD diffraction peaks were in agreement with the diffraction pattern of $PbMoO_4$ crystals (JCPDS card No. 01-071-4910), confirming the conversion of MoS_2-N-H into $PbMoO_4$-like crystal structures (possibly as $PbMoO_{4-x}S_x$) (Figure 10a). The sharp, high-intensity peaks indicated the good crystallinity of the product. Furthermore, to confirm the formation of a new product after adsorption, the chemical states were examined using XPS (Figure 10b−f). The XPS survey demonstrated that the product consisted of the elements Pb, O, Mo, S, and C. The Pb, O, and Mo peaks had high intensities, while S had a low-intensity peak, suggesting that S was present as a dopant in the sample. The deconvoluted Pb 4f spectrum in Figure 10c exhibited peaks at 138.7 and 143.5 eV, which corresponded to Pb $4f_{7/2}$ and Pb $4f_{5/2}$, respectively, suggesting the occurrence of Pb^{2+} as Pb−O of the $PbMoO_{4-x}S_x$. The binding energy peak at 144.3 and 139.5 eV was related to Pb $4f_{5/2}$ and Pb $4f_{7/2}$, which occurred due to the existence of Pb^{2+} as Pb−S of the $PbMoO_{4-x}S_x$.[60,63] The both sets of peaks showed a separation gap of 4.8 eV, which reflected the strong binding between Pb and O/S atoms. The high-resolution spectrum of Mo 3d exhibited two pairs of doublet peaks that corresponded to the two kinds of oxidation states of Mo in $PbMoO_{4-x}S_x$ (Figure 10d). One pair of peaks centered at 235.6 eV (Mo $3d_{3/2}$) and 232.7 eV (Mo $3d_{5/2}$) corresponded to the Mo(VI) oxidation state in $PbMoO_{4-x}S_x$, whereas another pair of peaks appeared at the lower binding energies of 232.4 and 235.5 eV, representing the Mo(V) oxidation state.[63,64] Figure 10e depicts the XPS spectrum of O 1s; the peak centered at 530.5 eV represents the Pb−O bond. The additional peaks at 531.8 and 533.2 eV were assigned to C−

DOI: 10.1021/acsami.9b03853
ACS Appl. Mater. Interfaces 2019, 11, 19141−19155

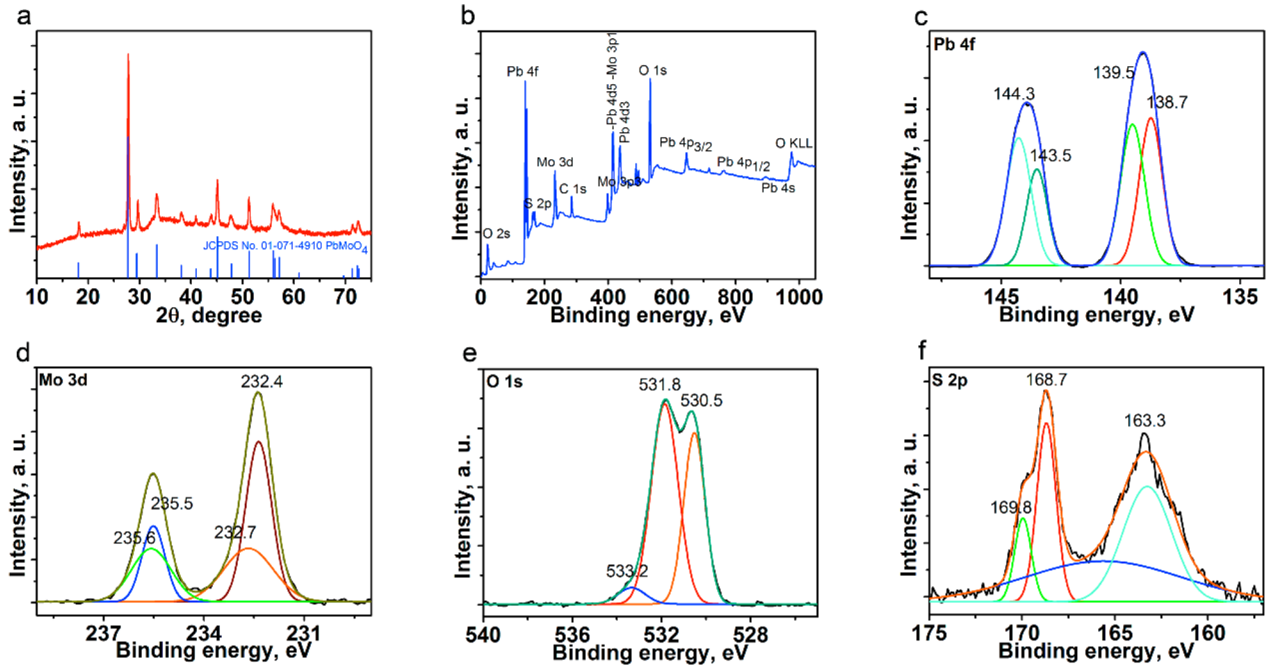

Figure 10. (a) XRD pattern. (b) XPS survey spectrum and deconvoluted spectra of (c) Pb 4f, (d) Mo 3d, (e) O 1s, and (f) S 2p of the spent adsorbent MoS_2-N-H after the removal of Pb(II) ions.

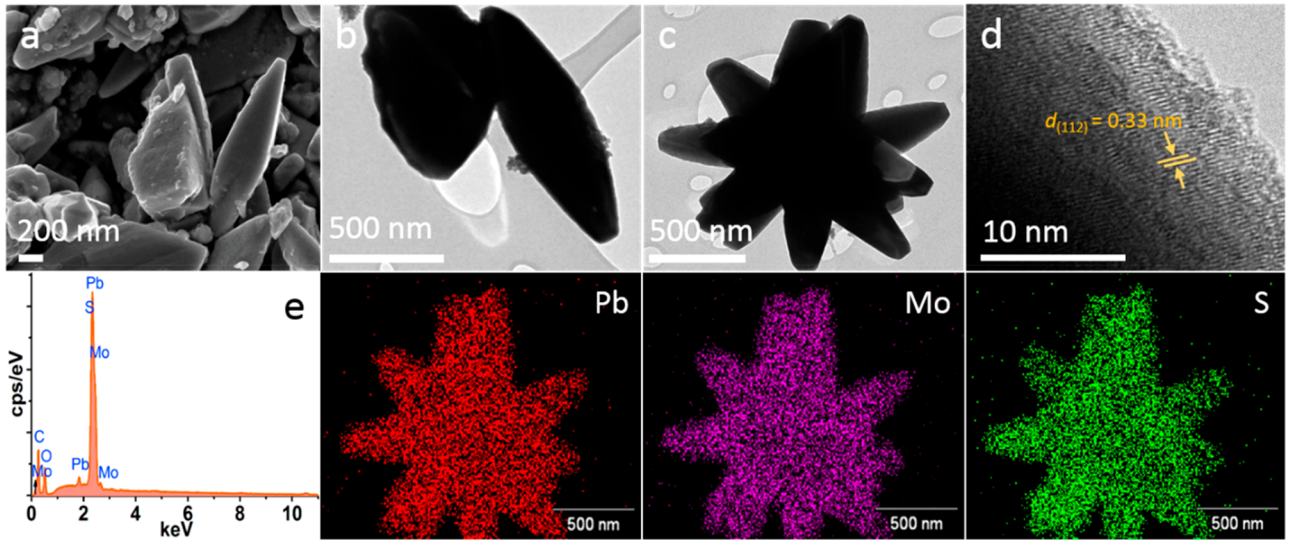

Figure 11. (a) SEM image, (b, c) TEM images, (d) HRTEM image with the lattice fringes highlighted, and (e) EDX spectrum and EDX mapping images of $PbMoO_{4-x}S_x$.

O and M−C−O linkages, respectively, which were already present in the original MoS_2-N-H sample.[58] Additionally, in the S 2p XPS spectrum (Figure 10f), the peak centered at 163.3 was associated with a Pb−S bond (S^{2-} state), which confirmed the presence of S as a dopant in $PbMoO_{4-x}S_x$. The high binding energy peaks at 168.7 eV ($2p_{3/2}$) and 169.8 ($2p_{3/2}$) corresponded to the high oxidation state S(VI) as sulfate, which originated from intercalated ions of MoS_2-N-H. The broad peak centered at 165.4 eV could be ascribed to bridging S_2^{2-}.[46]

The exterior and interior surface characteristics of $PbMoO_{4-x}S_x$ were investigated using SEM and TEM/HRTEM. In Figure 11a, the SEM image displays nanospindle-like structures with a width of 400−500 nm and a length of a few microns (~1.5 μm). Some structures that had not completely grown spindles were also observed (Figure 11b). These nanospindles joined together to construct microflower-like structures. Interestingly, the end edges of all the spindles/petals were blunt (not sharp), indicating the uniform formation of $PbMoO_{4-x}S_x$ (Figure 11b,c). As shown in Figure 11b, very small particles were anchored on the spindle, which might be composed of C (from MoS_2-N-H) or unconverted MoS_2 nanosheets. The HRTEM image (Figure 11d) exhibited a lattice spacing d of 0.33 nm, which corresponded to the (112) plane of $PbMoO_4$, suggesting the formation of the product $PbMoO_{4-x}S_x$ (lattice spacing calculation is shown in Figure S14, SI).[65] Moreover, the EDX results demonstrated that the obtained product was composed of all the expected elements, i.e., Mo, S, O, Pb, and C (Figure 11e), reaffirming the formation

DOI: 10.1021/acsami.9b03853
ACS Appl. Mater. Interfaces 2019, 11, 19141−19155

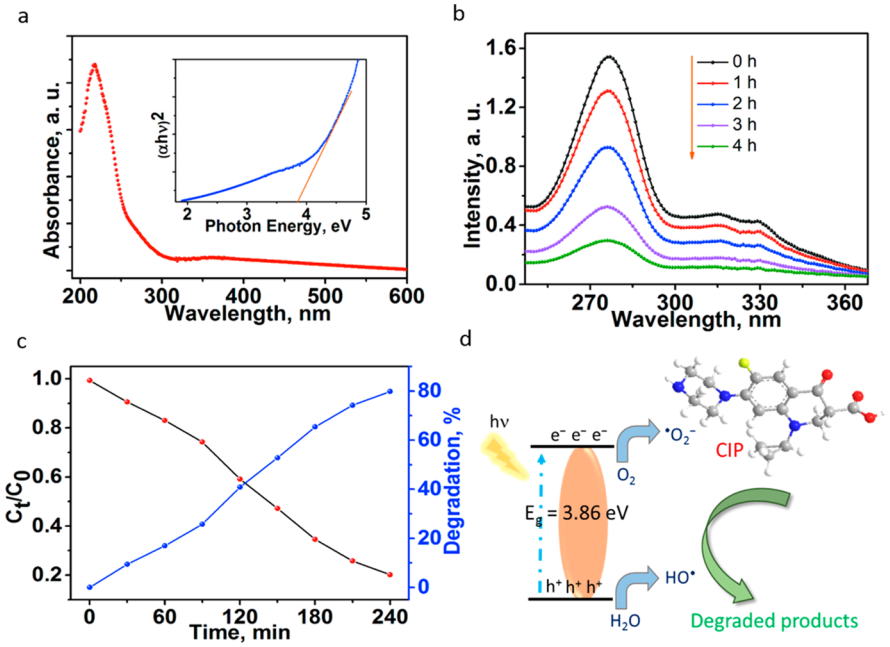

Figure 12. (a) UV−vis absorbance spectrum of $PbMoO_{4-x}S_x$; the inset is the Tauc plot for the band gap calculation. (b) Change in the UV−vis absorbance of CIP during irradiation. (c) Change in the concentration and photodegradation (%) of CIP with time. (d) Schematic depicting the photocatalytic mechanism of the degradation of CIP using $PbMoO_{4-x}S_x$ nanospindles.

of $PbMoO_{4-x}S_x$. Additionally, EDX mapping also showed the uniform distribution of Mo, S, and Pb throughout the sample.

The UV−vis absorbance spectrum of $PbMoO_{4-x}S_x$ is depicted in Figure 12a and shows an absorption edge at ∼319 nm. The broad band centered at 390 nm could be attributed to the presence of C moieties originating from MoS_2-N-H. As reported in the literature, molybdate is a direct band gap semiconductor and has a band gap value of ∼3.40 eV.[63] The band gap of $PbMoO_{4-x}S_x$ was calculated from the tangent to the x-axis in the Tauc plot of $(\alpha h\nu)^2$ vs $h\nu$ (energy) (see the inset of Figure 12a). The band gap of $PbMoO_{4-x}S_x$ was determined to be 3.86 eV, which can only be activated in UV light. The increase in the band gap value might be ascribed to the S-doping in the crystal structure of $PbMoO_4$.

Photocatalytic Degradation of CIP Using $PbMoO_{4-x}S_x$. The photocatalytic activity of $PbMoO_{4-x}S_x$ was investigated by measuring the degradation of CIP under UV−vis light irradiation. Initially, the photolysis experiment was executed in the absence of the photocatalyst with light irradiation. This control experiment demonstrated that no significant changes in the degradation of CIP occurred (∼9.4%) and also suggested that the degradation process of CIP mainly occurred via photocatalysis (Figure S15a, SI). As shown in Figure 12b, the absorbance intensity of CIP decreased with increasing reaction time, confirming the photocatalytic properties of the material. The amount of CIP was significantly reduced by treatment with the $PbMoO_{4-x}S_x$ nanospindles, and 79.8% photodegradation efficiency was obtained after 4 h in the presence of UV−vis light (Figure 12c). Moreover, for comparison, the photocatalytic efficiency of initial material (MoS_2-N-H) was observed (50.5%), which was lower than that of $PbMoO_{4-x}S_x$ nanospindles. The high photocatalytic efficiency of $PbMoO_{4-x}S_x$ toward CIP degradation was attributed to the high absorption of light and delayed recombination of the e^-/h^+ pairs. Furthermore, the kinetics of the degradation of CIP using the nanospindles was analyzed using the first-order kinetics reaction $\ln\left(\frac{C_0}{C_t}\right) = Kt$. In this equation, K signifies the rate constant (min^{-1}), t signifies time (min), and C_0 and C_t (mg/L) relate to the initial and final concentration of CIP. As shown in Figure S15b (SI), the plot of $\ln(C_0/C_t)$ versus t was linear, indicating that the obtained data was well-followed by first-order kinetics, and the rate constant was determined to be 0.0068 min^{-1}. Additionally, recycling experiments were conducted to check the reusability of $PbMoO_{4-x}S_x$ photocatalyst over four successive cycles under similar conditions (Figure S16, SI). No significant change occurred in degradation efficiency of CIP after four cycles, suggesting the reusability and stability of the catalyst.

The light-induced charged species and their migration are depicted schematically in Figure 12d. Under light irradiation, electron−hole pairs were produced on the surface of the $PbMoO_{4-x}S_x$ nanospindles. The generated electrons converted dissolved O_2 into superoxide oxygen ($^{\bullet}O_2^-$), while the holes participated in the conversion of water to hydroxyl radicals ($^{\bullet}OH$). At the same time, the strong polarization of Mo(VI) and Pb(II) initiated charge transmission between O_2^- and Mo(VI)/Pb(II) and resulted in enhanced photodegradation.[63] Furthermore, the dangling sulfur bonds in $PbMoO_{4-x}S_x$ also promoted degradation by providing catalytically active sites. The proposed charge transfer delayed the recombination of e^-/h^+ pairs, which led to high production of reactive oxygen species (ROS). Therefore, the presence of excess ROS, such as $^{\bullet}OH$ and $^{\bullet}O_2^-$, was responsible for the improved photocatalytic conversion of CIP to less toxic products.[47,64,66,67]

CONCLUSION

In summary, MoS_2 micro/nanostructures with new morphologies and increased interlayer spacing were synthesized via a single-step hydrothermal route using the new S source DDC in the presence of EDTA at different pH values. Microrods, microspheres, and microrods with hairlike structures were prepared from MoS_2 nanosheets at pH 7, pH 10, and pH 7 with a high concentration of DDC, respectively. The increased

DOI: 10.1021/acsami.9b03853
ACS Appl. Mater. Interfaces 2019, 11, 19141−19155

interlayer distance (~1.0 nm) in all the structures was ascribed to the presence of Na/hydrated Na and $Na_2SO_4/(NH_4)_2SO_4$, which originated from DDC and NaOH, between adjacent S−Mo−S layers, providing an abundance of accessible S adsorption sites. The FTIR spectra demonstrated the anchoring of EDTA on the MoS_2 nanostructures. Among the three nanostructures, MoS_2-N-H demonstrated an excellent capacity (303.04 mg/g) and high affinity for Pb(II). Its superior adsorption capacity was attributed to Pb−S complexation (strong Lewis base interactions) and electrostatic interactions between DDC/EDTA and Pb(II) ions. The adsorption was best fitted using the Freundlich isotherm and pseudo-second-order kinetics, suggesting a multilayer chemisorption process for adsorption of Pb(II) onto the MoS_2-N-H nanostructures. To evaluate their practical utility, the MoS_2-N-H nanostructures were employed in real mine water; the nanostructures successfully removed almost 100% of the Pb(II) ions in the presence of various coexisting ions, suggesting the high selectivity of the adsorbent. After careful characterization of the spent adsorbent using XRD, XPS, SEM/HRTEM, it was concluded that MoS_2-N-H was converted into $PbMoO_{4-x}S_x$ nanospindles. To avoid secondary waste, the $PbMoO_{4-x}S_x$ nanospindles were used for the photodegradation of the antibiotic CIP, and their high photodegradation efficiency (79.8%) was ascribed to the high amount of ROS production due to the delayed recombination of e^-/h^+ pairs. Thus, the developed MoS_2-N-H with increased interlayer spacing might represent a promising candidate for the uptake of Pb(II) in industrial applications.

■ ASSOCIATED CONTENT

Supporting Information

The Supporting Information is available free of charge on the ACS Publications website at DOI: 10.1021/acsami.9b03853.

Details of characterization tools used and photocatalytic studies; EDX mapping of MoS_2-N-H and MoS_2-DDC (0.932 g); SEM images for beam irradiation effects on hairlike structures and of MoS_2 synthesized in ethanol with DDC; XRD pattern for different DDC concentrations; XPS, surface area, and pore diameter of MoS_2-N, MoS_2-N-H, and MoS_2-B; ζ-potential at different pH values; adsorption isotherm plot; Temkin and DKR isotherms results; details of different kinetics models and calculated parameters; mine water composition; adsorption mechanism; d-spacing for $PbMoO_{4-x}S_x$; photodegradation percent and kinetics graphs; and recycling studies (PDF)

■ AUTHOR INFORMATION

Corresponding Authors

*N.K. e-mail: nkumar@csir.co.za, ynk.neeraj@gmail.com.
*S.S.R. e-mail: rsuprakas@csir.co.za, ssinharay@uj.ac.za.

ORCID

Neeraj Kumar: 0000-0001-5019-6329
Elvis Fosso-Kankeu: 0000-0002-7710-4401
Suprakas Sinha Ray: 0000-0002-0007-2595

Notes

The authors declare no competing financial interest.

■ ACKNOWLEDGMENTS

The authors would like to thank the Council for Scientific and Industrial Research (HGER74P) and Department of Science and Technology (HGERA8X) for financial support.

■ REFERENCES

(1) Li, Y.; Yang, Z.; Wang, Y.; Bai, Z.; Zheng, T.; Dai, X.; Liu, S.; Gui, D.; Liu, W.; Chen, M.; Chen, L.; Diwu, J.; Zhu, L.; Zhou, R.; Chai, Z.; Albrecht-Schmitt, T. E.; Wang, S. A Mesoporous Cationic Thorium-Organic Framework that Rapidly Traps Anionic Persistent Organic Pollutants. *Nat. Commun.* **2017**, *8*, 1354.

(2) Liu, W.; Dai, X.; Bai, Z.; Wang, Y.; Yang, Z.; Zhang, L.; Xu, L.; Chen, L.; Li, Y.; Gui, D.; Diwu, J.; Wang, J.; Zhou, R.; Chai, Z.; Wang, S. Highly Sensitive and Selective Uranium Detection in Natural Water Systems Using a Luminescent Mesoporous Metal−Organic Framework Equipped with Abundant Lewis Basic Sites: A Combined Batch, X-ray Absorption Spectroscopy, and First Principles Simulation Investigation. *Environ. Sci. Technol.* **2017**, *51*, 3911−3921.

(3) Gu, P.; Xing, J.; Wen, T.; Zhang, R.; Wang, J.; Zhao, G.; Hayat, T.; Ai, Y.; Lin, Z.; Wang, X. Experimental and Theoretical Calculation Investigation on Efficient Pb(II) Adsorption on Etched Ti_3AlC_2 Nanofibers and Nanosheets. *Environ. Sci.: Nano* **2018**, *5*, 946−955.

(4) Abbaspour, A.; Mirahmadi, E.; Khalafi-nejad, A.; Babamohammadi, S. A Highly Selective and Sensitive Disposable Carbon Composite PVC-Based Membrane for Determination of Lead Ion in Environmental Samples. *J. Hazard. Mater.* **2010**, *174*, 656−661.

(5) Wang, J.; Wang, P.; Wang, H.; Dong, J.; Chen, W.; Wang, X.; Wang, S.; Hayat, T.; Alsaedi, A.; Wang, X. Preparation of Molybdenum Disulfide Coated Mg/Al Layered Double Hydroxide Composites for Efficient Removal of Chromium(VI). *ACS Sustainable Chem. Eng.* **2017**, *5* (8), 7165−7174.

(6) Medina, R. P.; Nadres, E. T.; Ballesteros, F. C.; Rodrigues, D. F. Incorporation of Graphene Oxide into a Chitosan−Poly(Acrylic Acid) Porous Polymer Nanocomposite for Enhanced Lead Adsorption. *Environ. Sci.: Nano* **2016**, *3*, 638−646.

(7) Wan, S.; He, F.; Wu, J.; Wan, W.; Gu, Y.; Gao, B. Rapid and Highly Selective Removal of Lead from Water using Graphene Oxide-Hydrated Manganese Oxide Nanocomposites. *J. Hazard. Mater.* **2016**, *314*, 32−40.

(8) Lingamdinne, L. P.; Chang, Y.-Y.; Yang, J.-K.; Singh, J.; Choi, E.-H.; Shiratani, M.; Koduru, J. R.; Attri, P. Biogenic Reductive Preparation of Magnetic Inverse Spinel Iron Oxide Nanoparticles for the Adsorption Removal of Heavy Metals. *Chem. Eng. J.* **2017**, *307*, 74−84.

(9) Pei, H.; Wang, J.; Yang, Q.; Yang, W.; Hu, N.; Suo, Y.; Zhang, D.; Li, Z.; Wang, J. Interfacial Growth of Nitrogen-Doped Carbon with Multi-Functional Groups on the MoS_2 Skeleton for Efficient Pb(II) Removal. *Sci. Total Environ.* **2018**, *631−632*, 912−920.

(10) Yin, N.; Wang, K.; Wang, L.; Li, Z. Amino-Functionalized MOFs Combining Ceramic Membrane Ultrafiltration for Pb (II) Removal. *Chem. Eng. J.* **2016**, *306*, 619−628.

(11) Ali, I. New Generation Adsorbents for Water Treatment. *Chem. Rev.* **2012**, *112*, 5073−5091.

(12) Daneshyar, A.; Ghaedi, M.; Sabzehmeidani, M. M.; Daneshyar, A. H_2S Adsorption onto Cu-Zn−Ni Nanoparticles Loaded Activated Carbon and Ni-Co Nanoparticles Loaded γ-Al_2O_3: Optimization and Adsorption Isotherms. *J. Colloid Interface Sci.* **2017**, *490*, 553−561.

(13) Zhu, H.; Yuan, J.; Tan, X.; Zhang, W.; Fang, M.; Wang, X. Efficient Removal of Pb^{2+} by Tb-MOFs: Identifying the Adsorption Mechanism Through Experimental and Theoretical Investigations. *Environ. Sci.: Nano* **2019**, *6*, 261−272.

(14) Xu, Q.; Wang, Y.; Jin, L.; Wang, Y.; Qin, M. Adsorption of Cu (II), Pb (II) And Cr (VI) from Aqueous Solutions Using Black Wattle Tannin-Immobilized Nanocellulose. *J. Hazard. Mater.* **2017**, *339*, 91−99.

(15) Jiang, M.-q.; Jin, X.-y.; Lu, X.-Q.; Chen, Z.-l. Adsorption of Pb(II), Cd(II), Ni(II) and Cu(II) onto Natural Kaolinite Clay. *Desalination* **2010**, *252*, 33−39.

DOI: 10.1021/acsami.9b03853
ACS Appl. Mater. Interfaces 2019, 11, 19141−19155

(16) Manzoor, Q.; Nadeem, R.; Iqbal, M.; Saeed, R.; Ansari, T. M. Organic Acids Pretreatment Effect on Rosa Bourbonia Phyto-Biomass for Removal of Pb(II) And Cu(II) from Aqueous Media. *Bioresour. Technol.* **2013**, *132*, 446−452.
(17) Li, F.; Wang, X.; Yuan, T.; Sun, R. A Lignosulfonate-Modified Graphene Hydrogel with Ultrahigh Adsorption Capacity for Pb(II) Removal. *J. Mater. Chem. A* **2016**, *4*, 11888−11896.
(18) Wen, X.; Shao, C.-T.; Chen, W.; Lei, Y.; Ke, Q.-F.; Guo, Y.-P. Mesoporous Carbonated Hydroxyapatite/Chitosan Porous Materials for Removal of Pb(II) Ions Under Flow Conditions. *RSC Adv.* **2016**, *6*, 113940−113950.
(19) Ma, S.; Zhan, S.; Jia, Y.; Zhou, Q. Highly Efficient Antibacterial and Pb(II) Removal Effects of Ag-$CoFe_2O_4$-GO Nanocomposite. *ACS Appl. Mater. Interfaces* **2015**, *7*, 10576−10586.
(20) Liu, Z.; Fang, Y.; Jia, H.; Wang, C.; Song, Q.; Li, L.; Lin, J.; Huang, Y.; Yu, C.; Tang, C. Novel Multifunctional Cheese-Like 3D Carbon-BN as a Highly Efficient Adsorbent for Water Purification. *Sci. Rep.* **2018**, *8*, 1104.
(21) Wang, Z.; Mi, B. Environmental Applications of 2D Molybdenum Disulfide (MoS_2) Nanosheets. *Environ. Sci. Technol.* **2017**, *51*, 8229−8244.
(22) Umukoro, E. H.; Kumar, N.; Ngila, J. C.; Arotiba, O. A. Expanded Graphite Supported p-n MoS_2-SnO_2 Heterojunction Nanocomposite Electrode for Enhanced Photo-Electrocatalytic Degradation of A Pharmaceutical Pollutant. *J. Electroanal. Chem.* **2018**, *827*, 193−203.
(23) Chen, Y.; Chen, L.; Bai, H.; Li, L. Graphene Oxide−Chitosan Composite Hydrogels as Broad-Spectrum Adsorbents for Water Purification. *J. Mater. Chem. A* **2013**, *1*, 1992−2001.
(24) Upadhyay, R. K.; Soin, N.; Roy, S. S. Role of Graphene/Metal Oxide Composites as Photocatalysts, Adsorbents and Disinfectants in Water Treatment: A Review. *RSC Adv.* **2014**, *4*, 3823−3851.
(25) Massey, A. T.; Gusain, R.; Kumari, S.; Khatri, O. P. Hierarchical Microspheres of MoS_2 Nanosheets: Efficient and Regenerative Adsorbent for Removal of Water-Soluble Dyes. *Ind. Eng. Chem. Res.* **2016**, *55*, 7124−7131.
(26) Wang, J.; Zhang, W.; Yue, X.; Yang, Q.; Liu, F.; Wang, Y.; Zhang, D.; Li, Z.; Wang, J. One-Pot Synthesis of Multifunctional Magnetic Ferrite−MoS_2−Carbon Dot Nanohybrid Adsorbent for Efficient Pb(II) Removal. *J. Mater. Chem. A* **2016**, *4*, 3893−3900.
(27) Ma, L.; Wang, Q.; Islam, S. M.; Liu, Y.; Ma, S.; Kanatzidis, M. G. Highly Selective and Efficient Removal of Heavy Metals by Layered Double Hydroxide Intercalated with the MoS_4^{2-} Ion. *J. Am. Chem. Soc.* **2016**, *138*, 2858−2866.
(28) Lee, C.; Yan, H.; Brus, L. E.; Heinz, T. F.; Hone, J.; Ryu, S. Anomalous Lattice Vibrations of Single- and Few-Layer MoS_2. *ACS Nano* **2010**, *4*, 2695−2700.
(29) Ai, K.; Ruan, C.; Shen, M.; Lu, L. MoS_2 Nanosheets with Widened Interlayer Spacing for High-Efficiency Removal of Mercury in Aquatic Systems. *Adv. Funct. Mater.* **2016**, *26*, 5542−5549.
(30) Li, X.-L.; Li, Y.-D. MoS_2 Nanostructures: Synthesis and Electrochemical Mg^{2+} Intercalation. *J. Phys. Chem. B* **2004**, *108*, 13893−13900.
(31) Kumar, N.; George, B. P. A.; Abrahamse, H.; Parashar, V.; Ngila, J. C. Sustainable One-Step Synthesis of Hierarchical Microspheres of PEGylated MoS_2 Nanosheets and MoO_3 Nanorods: Their Cytotoxicity Towards Lung and Breast Cancer Cells. *Appl. Surf. Sci.* **2017**, *396*, 8−18.
(32) Han, B.; Liu, S.; Zhang, N.; Xu, Y.-J.; Tang, Z.-R. One-Dimensional CdS@MoS_2 Core-Shell Nanowires for Boosted Photocatalytic Hydrogen Evolution Under Visible Light. *Appl. Catal., B* **2017**, *202*, 298−304.
(33) Wei, W.; Samad, L.; Choi, J. W.; Joo, Y.; Way, A.; Arnold, M. S.; Jin, S.; Gopalan, P. Synthesis of Molybdenum Disulfide Nanowire Arrays Using a Block Copolymer Template. *Chem. Mater.* **2016**, *28*, 4017−4023.
(34) Abu-El-Halawa, R.; Zabin, S. A. Removal Efficiency of Pb, Cd, Cu and Zn from Polluted Water Using Dithiocarbamate Ligands. *J. Taibah Univ. Sci.* **2017**, *11*, 57−65.
(35) Xie, J.; Zhang, J.; Li, S.; Grote, F.; Zhang, X.; Zhang, H.; Wang, R.; Lei, Y.; Pan, B.; Xie, Y. Controllable Disorder Engineering in Oxygen-Incorporated MoS_2 Ultrathin Nanosheets for Efficient Hydrogen Evolution. *J. Am. Chem. Soc.* **2013**, *135*, 17881−17888.
(36) Chatti, M.; Gengenbach, T.; King, R.; Spiccia, L.; Simonov, A. N. Vertically Aligned Interlayer Expanded MoS_2 Nanosheets on a Carbon Support for Hydrogen Evolution Electrocatalysis. *Chem. Mater.* **2017**, *29*, 3092−3099.
(37) Chen, L.; Feng, Y.; Zhou, X.; Zhang, Q.; Nie, W.; Wang, W.; Zhang, Y.; He, C. One-Pot Synthesis of MoS_2 Nanoflakes with Desirable Degradability for Photothermal Cancer Therapy. *ACS Appl. Mater. Interfaces* **2017**, *9*, 17347−17358.
(38) Chen, J.; Shi, Y.-e.; Zhang, M.; Zhan, J. Diethyldithiocarbamate (DDTC) Induced Formation of Positively Charged Silver Nanoparticles for Rapid in Situ Identification of Inorganic Explosives by Surface Enhanced Raman Spectroscopy. *RSC Adv.* **2016**, *6*, 51823−51829.
(39) Gao, M.-R.; Chan, M. K. Y.; Sun, Y. Edge-Terminated Molybdenum Disulfide with a 9.4-Å Interlayer Spacing for Electrochemical Hydrogen Production. *Nat. Commun.* **2015**, *6*, 7493.
(40) Anjum, M. A. R.; Jeong, H. Y.; Lee, M. H.; Shin, H. S.; Lee, J. S. Efficient Hydrogen Evolution Reaction Catalysis in Alkaline Media by All-in-One MoS_2 with Multifunctional Active Sites. *Adv. Mater.* **2018**, *30*, 1707105.
(41) Lin, C.-H.; Tsai, C.-H.; Tseng, F.-G.; Yu, Y.-Y.; Wu, H.-C.; Hsieh, C.-K. Low-Temperature Thermally Reduced Molybdenum Disulfide as a Pt-Free Counter Electrode for Dye-Sensitized Solar Cells. *Nanoscale Res. Lett.* **2015**, *10*, 446.
(42) Kumar, N.; George, B. P. A.; Abrahamse, H.; Parashar, V.; Ray, S. S.; Ngila, J. C. A Novel Approach to Low-Temperature Synthesis of Cubic HfO_2 Nanostructures and Their Cytotoxicity. *Sci. Rep.* **2017**, *7*, 9351.
(43) Kumar, N.; Reddy, L.; Parashar, V.; Ngila, J. C. Controlled Synthesis of Microsheets of ZnAl Layered Double Hydroxides Hexagonal Nanoplates for Efficient Removal of Cr(VI) Ions and Anionic Dye from Water. *J. Environ. Chem. Eng.* **2017**, *5*, 1718−1731.
(44) Kumar, D.; Singh, M.; Ramanan, A. Crystallization of Mo−EDTA Complex Based Solids: Molecular Insights. *J. Mol. Struct.* **2012**, *1030*, 89−94.
(45) Kloubek, J.; Podlaha, J. Molybdenum(III) Complexes of Ethylenediaminetetraacetic Acid. *J. Inorg. Nucl. Chem.* **1971**, *33*, 2981−2988.
(46) Cao, P.; Peng, J.; Liu, S.; Cui, Y.; Hu, Y.; Chen, B.; Li, J.; Zhai, M. Tuning the Composition and Structure of Amorphous Molybdenum Sulfide/Carbon Black Nanocomposites by Radiation Technique for Highly Efficient Hydrogen Evolution. *Sci. Rep.* **2017**, *7*, 16048.
(47) Kumar, N.; Mittal, H.; Alhassan, S. M.; Ray, S. S. Bionanocomposite Hydrogel for the Adsorption of Dye and Reusability of Generated Waste for the Photodegradation of Ciprofloxacin: A Demonstration of the Circularity Concept for Water Purification. *ACS Sustainable Chem. Eng.* **2018**, *6*, 17011−17025.
(48) Liao, W.-H.; Yang, S.-Y.; Hsiao, S.-T.; Wang, Y.-S.; Li, S.-M.; Ma, C.-C. M.; Tien, H.-W.; Zeng, S.-J. Effect of Octa(aminophenyl) Polyhedral Oligomeric Silsesquioxane Functionalized Graphene Oxide on the Mechanical and Dielectric Properties of Polyimide Composites. *ACS Appl. Mater. Interfaces* **2014**, *6*, 15802−15812.
(49) Zhang, X.; Yang, S.; Yu, B.; Tan, Q.; Zhang, X.; Cong, H. Advanced Modified Polyacrylonitrile Membrane with Enhanced Adsorption Property for Heavy Metal Ions. *Sci. Rep.* **2018**, *8*, 1260.
(50) Li, L.; Qu, Q.; Bai, W.; Yang, F.; Chen, Y.; Zhang, S.; Ding, Z. Sodium Diethyldithiocarbamate as a Corrosion Inhibitor of Cold Rolled Steel in 0.5M Hydrochloric Acid Solution. *Corros. Sci.* **2012**, *59*, 249−257.
(51) Otyepková, E.; Lazar, P.; Luxa, J.; Berka, K.; Čépe, K.; Sofer, Z.; Pumera, M.; Otyepka, M. Surface Properties of MoS_2 Probed By Inverse Gas Chromatography and Their Impact on Electrocatalytic Properties. *Nanoscale* **2017**, *9*, 19236−19244.

DOI: 10.1021/acsami.9b03853
ACS Appl. Mater. Interfaces 2019, 11, 19141−19155

(52) Paek, S.-M.; Jung, H.; Park, M.; Lee, J.-K.; Choy, J.-H. An Inorganic Nanohybrid with High Specific Surface Area: TiO_2-Pillared MoS_2. *Chem. Mater.* **2005**, *17*, 3492−3498.
(53) Jiang, X.; Luo, H.; Yin, Y.; Zhou, W. Facile Synthesis of MoS_2/Reduced Graphene Oxide Composites for Efficient Removal of Cr(VI) from Aqueous Solutions. *RSC Adv.* **2017**, *7*, 24149−24156.
(54) Ding, C.; Cheng, W.; Wang, X.; Wu, Z.-Y.; Sun, Y.; Chen, C.; Wang, X.; Yu, S.-H. Competitive Sorption of Pb(II), Cu(II) And Ni(II) on Carbonaceous Nanofibers: A Spectroscopic and Modeling Approach. *J. Hazard. Mater.* **2016**, *313*, 253−261.
(55) Roosta, M.; Ghaedi, M.; Daneshfar, A.; Sahraei, R.; Asghari, A. Optimization of Combined Ultrasonic Assisted/Tin Sulfide Nanoparticle Loaded on Activated Carbon Removal of Erythrosine By Response Surface Methodology. *J. Ind. Eng. Chem.* **2015**, *21*, 459−469.
(56) Du, Y.; Wang, J.; Zou, Y.; Yao, W.; Hou, J.; Xia, L.; Peng, A.; Alsaedi, A.; Hayat, T.; Wang, X. Synthesis of Molybdenum Disulfide/Reduced Graphene Oxide Composites for Effective Removal of Pb(II) from Aqueous Solutions. *Sci. Bull.* **2017**, *62*, 913−922.
(57) Aghagoli, M. J.; Shemirani, F. Hybrid Nanosheets Composed of Molybdenum Disulfide and Reduced Graphene Oxide for Enhanced Solid Phase Extraction of Pb(II) and Ni(II). *Microchim. Acta* **2017**, *184*, 237−244.
(58) Zhu, H.; Tan, X.; Tan, L.; Chen, C.; Alharbi, N. S.; Hayat, T.; Fang, M.; Wang, X. Biochar Derived from Sawdust Embedded with Molybdenum Disulfide for Highly Selective Removal of Pb^{2+}. *ACS Appl. Nano Mater.* **2018**, *1*, 2689−2698.
(59) Sharifpour, E.; Khafri, H. Z.; Ghaedi, M.; Asfaram, A.; Jannesar, R. Isotherms and Kinetic Study of Ultrasound-Assisted Adsorption of Malachite Green and Pb^{2+} Ions from Aqueous Samples by Copper Sulfide Nanorods Loaded on Activated Carbon: Experimental Design Optimization. *Ultrason. Sonochem.* **2018**, *40*, 373−382.
(60) Kong, L.; Yan, L.; Qu, Z.; Yan, N.; Li, L. β-Cyclodextrin Stabilized Magnetic Fe_3S_4 Nanoparticles for Efficient Removal of Pb(II). *J. Mater. Chem. A* **2015**, *3*, 15755−15763.
(61) Xie, L.; Yu, Z.; Islam, S. M.; Shi, K.; Cheng, Y.; Yuan, M.; Zhao, J.; Sun, G.; Li, H.; Ma, S.; Kanatzidis, M. G. Remarkable Acid Stability of Polypyrrole-MoS_4: A Highly Selective and Efficient Scavenger of Heavy Metals Over a Wide pH Range. *Adv. Funct. Mater.* **2018**, *28*, 1800502.
(62) Jia, F.; Zhang, X.; Song, S. AFM Study on the Adsorption of Hg^{2+} on Natural Molybdenum Disulfide in Aqueous Solutions. *Phys. Chem. Chem. Phys.* **2017**, *19*, 3837−3844.
(63) Du, W.; Liu, L.; Zhou, K.; Ma, X.; Hao, Y.; Qian, X. Black Lead Molybdate Nanoparticles: Facile Synthesis and Photocatalytic Properties Responding to Visible Light. *Appl. Surf. Sci.* **2015**, *328*, 428−435.
(64) Datta, R. S.; Ou, J. Z.; Mohiuddin, M.; Carey, B. J.; Zhang, B. Y.; Khan, H.; Syed, N.; Zavabeti, A.; Haque, F.; Daeneke, T.; Kalantar-zadeh, K. Two Dimensional $PbMoO_4$: A Photocatalytic Material Derived from a Naturally Non-layered Crystal. *Nano Energy* **2018**, *49*, 237−246.
(65) Mondal, B.; Mahendranath, A.; Som, A.; Bose, S.; Ahuja, T.; Kumar, A. A.; Ghosh, J.; Pradeep, T. Rapid Reaction of MoS_2 Nanosheets with Pb^{2+} And Pb^{4+} Ions in Solution. *Nanoscale* **2018**, *10*, 1807−1814.
(66) Kumar, N.; Sinha Ray, S.; Ngila, J. C. Ionic Liquid-Assisted Synthesis of Ag/Ag_2Te Nanocrystals via a Hydrothermal Route for Enhanced Photocatalytic Performance. *New J. Chem.* **2017**, *41*, 14618−14626.
(67) Kumar, N.; Mittal, H.; Reddy, L.; Nair, P.; Ngila, J. C.; Parashar, V. Morphogenesis of ZnO Nanostructures: Role of Acetate ($COOH^-$) and Nitrate (NO_3^-) Ligand Donors from Zinc Salt Precursors in Synthesis and Morphology Dependent Photocatalytic Properties. *RSC Adv.* **2015**, *5*, 38801−38809.

DOI: 10.1021/acsami.9b03853
ACS Appl. Mater. Interfaces 2019, 11, 19141−19155